Interaction between Ventricular Expansion and Structural Changes in the Corpus Callosum and Putamen in Males with *FMR1* Normal and Premutation Alleles

Jun Yi Wang[a,b,c], **David Hessl**[b,d], **Flora Tassone**[b,c], **Kyoungmi Kim**[b,e], **Randi J. Hagerman**[b,f], **Susan M. Rivera**[a,b,g]

[a]Center for Mind and Brain, University of California-Davis, Davis, CA 95618

[b]MIND Institute, University of California-Davis Medical Center, Sacramento, CA 95817

[c]Department of Biochemistry and Molecular Medicine, University of California-Davis, School of Medicine, Sacramento, CA 95817

[d]Department of Psychiatry and Behavioral Sciences, University of California-Davis, School of Medicine, Sacramento, CA 95817

[e]Department of Public Health Sciences, University of California-Davis, School of Medicine, Sacramento, CA 95817

[f]Department of Pediatrics, University of California-Davis, School of Medicine, Sacramento, CA 95817

[g]Department of Psychology, University of California-Davis, Davis, CA 95616

Abstract

Ventricular enlargement (VE) is commonly observed in aging and fragile X-associated tremor/ataxia syndrome (FXTAS), a late-onset neurodegenerative disorder. VE may generate a mechanical force causing structural deformation. In this longitudinal study, we examined the relationships between VE and structural changes in the corpus callosum (CC) and putamen. MRI scans (2–7/person over 0.2–7.5 years) were acquired from 22 healthy controls, 26 unaffected premutation carriers (PFX–), and 39 carriers affected with FXTAS (PFX+). Compared with controls, PFX– demonstrated enlarged fourth ventricles whereas PFX+ displayed enlargement in both third and fourth ventricles, CC thinning, putamen atrophy/deformation (thinning and increased distance), and accelerated expansions in lateral ventricles. Common for all groups, baseline VE predicted accelerated CC thinning and putamen atrophy/deformation and conversely, baseline CC and putamen atrophy/deformation and enlarged third and fourth ventricles predicted accelerated lateral ventricular expansion. The results suggest a progressive VE within the four

Correspondence: Jun Yi Wang, **Address:** Center for Mind and Brain, 267 Cousteau Place, Davis, CA 95618, **Phone:** 530.747.3802, *Fax*: 530.297.4603, jyiwang@ucdavis.edu.

ventricles as FXTAS develops and a deleterious cycle between VE and brain deformation that may commonly occur during aging and FXTAS progression but become accelerated in FXTAS.

Keywords

fragile X premutation; FXTAS; *FMR1*; normal pressure hydrocephalus; MRI; neurodegenerative disorder

1. Introduction

The fragile X premutation is defined as a 55–200 CGG expansion in the 5' non-coding region of the fragile X mental retardation 1 (*FMR1*) gene and is associated with a late-onset progressive neurodegenerative disorder, fragile X-associated tremor/ataxia syndrome (FXTAS) (Hagerman *et al.*, 2001, Hagerman and Hagerman, 2013). Approximately 45% of male and 16% of female *FMR1* premutation carriers are affected by FXTAS after the age of 50. Those with FXTAS present a spectrum of clinical features, including intention tremor, cerebellar ataxia, parkinsonism, executive dysfunction, and memory deficits (Hagerman *et al.*, 2001, Hagerman and Hagerman, 2015). Subtle structural changes have been detected in premutation carriers without a clinical diagnosis of FXTAS (PFX−) in the cerebellum and brainstem (Hashimoto *et al.*, 2011, Wang *et al.*, 2012, Battistella *et al.*, 2013). Structural damage becomes substantial and widespread in premutation carriers with FXTAS (PFX+), to include generalized brain atrophy, thinning of the corpus callosum (CC), and ventricular enlargement (VE) (Brunberg *et al.*, 2002, Wang *et al.*, 2017).

VE is traditionally thought to be a passive consequence of brain atrophy in normal aging and neurodegenerative diseases (Nestor *et al.*, 2008, Apostolova *et al.*, 2012). However, circulation of cerebrospinal fluid (CSF) requires a balanced CSF secretion and outflow (Simon and Iliff, 2016). A small amount of pressure difference between the ventricles (the major site of CSF production) and subarachnoid spaces (the major site of CSF reabsorption) can be sufficient to initiate and sustain VE (Levine, 2008). In a dog model of normal pressure hydrocephalus (NPH), kaolin injection leads to a blockage of CSF reabsorption at the subarachnoid spaces. The result is increased intracranial pressure pulsatility and VE without atrophy and substantially elevated transmantle pressure between the ventricles and the subarachnoid spaces (Linninger *et al.*, 2005). Indeed, reduction in CSF venous outflow has been detected in normal aging (Albeck *et al.*, 1998, Satow *et al.*, 2017). Coupled with age-related decrease in tissue elasticity, these changes can lead to VE in the absence of substantially elevated transmantle pressure (Pena *et al.*, 2002, Keong *et al.*, 2016). Mechanical force generated by VE can potentially stretch or compress brain tissue, causing structural deformation and atrophy. The clinical symptoms can be gait disturbance, urinary incontinence, and dementia manifested as the neurological triad in NPH (Hakim and Adams, 1965). Consistently, thinning of the CC, a white matter structure that borders the lateral ventricles (LV), has been reported in FXTAS (Brunberg *et al.*, 2002), and the neurological triad of NPH overlaps with FXTAS symptomology (Hagerman *et al.*, 2008). We therefore hypothesize VE as a pathophysiologic process that exacerbates brain deformation and atrophy in FXTAS.

Both periventricular and non-periventricular structures can be affected as the mechanical force from VE may transit across brain tissues. Therefore, we selected two structures-of-interest, namely the CC, a periventricular white matter structure, and the putamen, a shell-shaped non-periventricular gray matter structure. Being metabolically active, the putamen is rich in mitochondria and vascular supply, and shows atrophy and robust age-related iron accumulation in aging (Fujii *et al.*, 2007, Cherubini *et al.*, 2009) and neurodegenerative diseases (de Jong *et al.*, 2008, Acosta-Cabronero *et al.*, 2013). In patients with FXTAS, atrophy and potential iron depositions in the putamen beyond normal aging have been demonstrated in *in vivo* MRI and then confirmed in a postmortem examination (Wang *et al.*, 2013b, Ariza *et al.*, 2017). Iron depositions were observed in capillaries and major cell types in the putamen affecting particularly the neurons and oligodendrocytes. However, the underlying physiologic mechanism remains elusive. One possibility is that the pressure generated by VE may squeeze the cells and distort the vasculature, causing deformation and iron depositions upon cell death. We hypothesized that the morphology of both CC and putamen would be affected by VE during FXTAS development and progression and tested this hypothesis in a longitudinal study of males with normal and premutation alleles of the *FMR1* gene.

2. Material and methods

2.1 Research participant

Research participants were recruited between 2009 and 2017 by two on-going longitudinal studies. All participants provided written informed consent before participation in line with the Declaration of Helsinki. The studies were conducted following procedures approved by the University of California Davis Institutional Review Board. We included 87 male participants (age 40 years) who completed >1 visit and MRI scans were acquired with acceptable quality (*i.e.*, no or minor motion artifacts that would not potentially have a notable effect on MRI quantifications) determined by an experienced neuroimaging researcher (JYW). One neurologically and neuropsychologically normal control had a lesion in the CC. This participant was excluded from all analyses involving the CC.

CGG repeat size was determined from genomic DNA isolated from peripheral blood lymphocytes using a combination of PCR and Southern blot Analysis as previously described (Tassone *et al.*, 2008, Filipovic-Sadic *et al.*, 2010). Total cellular RNA was purified from 2.5 ml peripheral blood where *FMR1* mRNA expression levels were measured by quantitative Real Time PCR using a 7900 Sequence detector (PE Biosystems) as previously described (Tassone *et al.*, 2000). Of the 87 participants, 22 carried normal alleles of the *FMR1* gene while 65 carried premutation alleles.

All research participants went through detailed assessment during each visit in the domains of clinic, neurology, psychology, and psychiatry. FXTAS severity was scored by a trained physician (RJH) using FXTAS stage (Bacalman *et al.*, 2006) based on the severities of movement and gait impairments. Carriers with FXTAS stage 0 or 1 at all visits ($N = 26$, no or equivocal tremor/ataxia) were classified as PFX− while those with FXTAS stage 2 and above at all visits ($N = 39$, clear tremor/ataxia with minor to severe interference of daily living) were classified as PFX+. See Table 1 for demographic information.

2.2 MRI acquisition and analysis

MRI scans were acquired on a Siemens Trio 3T MRI scanner equipped with a 32-channel head coil (Siemens Medical Solutions, Erlangen, Germany). One-mm isotropic T1-weighted scans were collected covering the whole brain using the magnetization-prepared rapid gradient-echo (MPRAGE) sequence in 192 sagittal slices, field of view of 256 mm^2, repetition time of 2170 ms, echo time of 4.86 ms, flip angle of 7°, inversion time of 1100 ms, and acquisition time of 8:06 minutes.

T1-weighted scans were aligned along the anterior-posterior commissure line automatically using the acpcdetect program from ART (www.nitrc.org/projects/art). For 39 failed cases (15.8% of 247 scans), the alignment was performed manually using DTI Studio (mristudio.org). MRI bias field correction was performed using N4 (Tustison *et al.*, 2010).

Brain segmentation was performed using the multiple-atlas likelihood fusion (MALF) algorithm implemented in BrainGPS (Tang *et al.*, 2013, Wang *et al.*, 2013a). The atlas used was the Adult50–90yrs_283Labels_19atlases_V9B, which provided segmentations for 283 regions in the two hemispheres, including the LV, 3rd ventricle (V3), 4th ventricle (V4), CC, and putamen. Segmentations of the ventricles and CC in the two hemispheres were combined, but were kept separate for the putamen. SegAdapter, a machine-learning based method (Wang *et al.*, 2011, Wang *et al.*, 2016), was used to automatically correct errors in all segmentations followed by manual correction by JYW using ITK-Snap (Yushkevich *et al.*, 2006). Volume calculation was performed using the fslstats command from FSL (Smith *et al.*, 2004).

We used the midsagittal slices to quantify CC morphology. The CC length and height were measured according to the published method using ITK-Snap (Weis *et al.*, 1993) (Fig. 1A). A single rater (JYW) obtained the measurements after achieving intra-rater reliability coefficients above 0.95. The CC thickness was calculated using an in-house R program (See A.1 in the Appendix for details and the program is available at https://github.com/jyiwang/CC_Thickness). Briefly, we used the midsagittal slices to quantify CC thickness. The upper and lower boundaries of the CC were determined along with the inflection points on the lower boundary (Fig. 1B, F). Then the CC was divided into sections by the lines connecting the inflection points and the middle of the voxels in the upper boundary that had the shortest distance to the inflection points (Fig. 1C, G). The 300 CC segments were formed by segmenting the upper boundary into 300 equal-length segments and segmenting the lower boundary into the same number of segments as the upper boundary in the same section. The CC thickness was calculated as the length of the line connecting the corresponding points on the upper and lower boundaries. Witelson's approach (Witelson, 1989) was applied to geometrically divide the CC into seven subregions comprising the rostrum (CC1), genu (CC2), rostral body (CC3), anterior midbody (CC4), posterior midbody (CC5), isthmus (CC6), and splenium (CC7) (Fig. 1D, H). Average thickness was calculated for each CC subregion as well as for the whole CC. In addition, we reduced the 300 CC segments to 60 to control number of comparisons for statistical analyses along each segment. The thickness of the 60 CC segments was calculated as the average thickness for every 5 segments.

Putamen morphology was measured on the axial slice above the anterior commissure. The 150 segmentations and thickness were computed similarly as the CC (see A.2 in the Appendix). The inner and outer distances between the left and right putamen were calculated as the length of the line linking the corresponding points on the inner or outer surfaces (Fig. 1I–L). The 150 segments were reduced to 30 segments for statistical analysis along the segments by computing the average values for every 5 segments. The average thickness and distance for the 150 segments was also calculated.

Since enlarged ventricles have been reported in FXTAS (Brunberg *et al.*, 2002, Cohen *et al.*, 2006), we followed the international guidelines of CT/MRI signs for NPH diagnosis and selection of shunt-responsive patients using Evans index (>0.3) and CC angle (<90°) (Ishii *et al.*, 2008). Briefly, Evans index was measured as the ratio of the maximum width of the frontal horns to the maximum width of the inner skull. The callosal angle was measured on the coronal slice showing the posterior commissure, which was also perpendicular to the anteroposterior commissure plane.

To account for individual differences in cranial size, we obtained brain scaling factors using the SIENAX (Smith *et al.*, 2002) program from FSL. The brain scaling factor is the determinant of the affine transformation of the brain and skull images to a standard space (Smith, 2002). It has shown a high correlation with manual total cranial volume (Buckner *et al.*, 2004) but is less affected by aging compared with total cranial volume generated automatically (Wang *et al.*, 2017).

2.3 Statistical analysis

Group differences in 13 MRI measures were compared, including 3 volume measurements from the ventricles (LV, V3, V4), 4 CC measurements (volume, length, height, and thickness), and 6 putamen measurements (left and right volume and thickness, inner distance, and outer distances). Mixed-effects models were constructed using group, age (time) at each visit, and their interaction as the predictors of interest and MRI data as the response variable. We also used mixed-effects models to examine the predictability of the baseline measure of one predictor variable (T1V) on the longitudinal change in the response variable of interest (V). A total of 60 models were evaluated comprising the use of the 3 baseline volumes of V3, V4 and LV for predicting changes in the 10 measurements from the CC and putamen, and the use of the 10 baseline measurements of the CC and putamen to predict volume changes in V3, V4, and LV. Model selection was carried out using a step-wise approach via likelihood ratio test among the following nested models with interaction terms in sequence:

1. $V = \text{intercept} + \text{group} + \text{age} + \text{T1V} + \text{age} \times \text{T1V} + \text{age} \times \text{group} + \text{age} \times \text{group} \times \text{T1V}$

2. $V = \text{intercept} + \text{group} + \text{age} + \text{T1V} + \text{age} \times \text{T1V} + \text{age} \times \text{group}$

3. $V = \text{intercept} + \text{group} + \text{age} + \text{T1V} + \text{age} \times \text{T1V}$

4. $V = \text{intercept} + \text{group} + \text{age} + \text{T1V}$

To understand the clinical importance of the observed MRI changes, associations between the 13 MRI measurements and FXTAS stage were estimated using mixed-effects models fitting FXTAS stage at each visit using the longitudinal MRI data and age. To investigate potential underlying molecular mechanisms the associations between the 13 MRI measurements and *FMR1* genetic markers were analyzed similarly fitting longitudinal MRI data in relation to CGG repeat length/*FMR1* mRNA level with FXTAS stage as a covariate, to account for the potential effect of disease severity on MRI data.

Brain scaling factor to account for individual differences in cranial size (Buckner *et al.*, 2004) was added as a covariate in all mixed-effects models involving volumes whereas the width of the inner skull (measured as a part of the Evan's index) served as a covariate for putamen distance. To maintain the family-wise Type 1 error rate at 0.05 for pairwise group comparisons, significance level was set at 0.017 (=0.05/3) using the Bonferroni correction for multiple group comparisons. In addition, the Benjamini-Hochberg method of false discovery rate (FDR) (Benjamini and Hochberg, 1995) was applied to control the FDR at 5% for all hypotheses tested in one type of analysis. All statistical analyses were conducted using the "nlme" package from the open-source statistical package R (http://www.r-project.org/).

3.   Results

The participants performed 2.5 visits on average (SD=0.8, range 2–7 visits) (Table 1). The average intervals between visits was 2.0 years (SD=1.1 years, range 0.2–7.3 years). While the age of the controls and PFX− was not significantly different ($t = 0.10$, $p = 0.92$), PFX+ was significantly older compared with both controls and PFX− (controls/PFX−: $t = 3.79/4.01$, both $p < 0.001$).

3.1   Majority of patients did not meet the diagnostic criteria for NPH

We examined whether any of the participants met diagnostic criteria for NPH using Evans index and CC angle (Ishii *et al.*, 2008). For Evans index, 19/39 PFX+, 2 PFX−, and 3 controls exceeded the threshold (>0.3). For CC angle, 4 PFX+, 2 PFX−, and 1 control met the criterion (<90°). Of these participants, 3 PFX+, 1 PFX−, and 1 control met both criteria of NPH (Table 1).

3.2   Progressive expansion from the V4 to the V3 and LV was observed in the premutation carriers

All MRI measurements except CC length showed a significant age effect, indicating that age-related VE and structural deformation and atrophy were common for all three groups (Table 2). A significant group effect was also detected indicating enlarged V4 in both PFX− and PFX+ compared with controls (PFX−/PFX+: $\beta = 0.64/0.92$ ml, FDR = 0.040/<0.001). In contrast, a significant group effect indicating enlarged V3 was only shown in PFX+ compared with controls ($\beta = 0.68$ ml, FDR = 0.003). For LV, only age by group interaction (with no group effect) reached statistical significance, indicating accelerated LV enlargement in PFX+ compared with both controls and PFX− (controls/PFX−: $\beta = 2.03/1.61$ ml/year, FDR < 0.001) (Table 2, Fig. 2A–C).

3.3 Only PFX+ (not PFX−) showed significant morphological changes in the CC and putamen compared with controls

While the PFX− group did not show any significant changes compared with controls, the PFX+ group demonstrated many significant changes in CC and putamen morphology (Table 2). The PFX+ group showed significant group effect, including CC thinning compared with both controls and PFX− (controls/PFX−: $\beta = -0.90/-0.60$ mm, FDR = 0.001/0.020), putamen atrophy (left/right $\beta = -0.45/-0.41$ ml, FDR = 0.003/0.010) and thinning at right side ($\beta = -0.39$ mm, FDR = 0.011) compared with controls, and putamen atrophy (left/right $\beta = -0.42/-0.36$ ml, FDR = 0.010/0.020) and thinning at right side ($\beta = -0.40$ mm, FDR = 0.013) compared with PFX−. Putamen inner distance was the only measurement that showed significant age by group interactions (with no group effect) in PFX+ compared with both controls and PFX− (controls/PFX−: $\beta = 0.13/0.12$ mm/year, FDR = 0.005/0.008). In contrast, CC volume, length, and height did not show any significant differences between the three groups (Fig. 2D–I).

The analysis of the 60 CC segments revealed significant age effect in all CC subregions (segments 1–40, 46–57, & 59, $t(126) = -5.97$--2.42, FDR <0.001–0.019, Fig. 3B). While PFX− did not show significant differences in CC thickness compared with controls, PFX+ demonstrated thinning most significantly in genu (CC2), rostral midbrain (CC3), and splenium (CC7) (segments 3–22, 25–26, 28, 37–38, 42, and 44–59, $t(83) = -2.53$--4.44, FDR <0.001–0.019, Fig. 3A, C, D). The comparisons of the seven CC subregions confirmed these results (Table 2). CC2 showed significant thinning in PFX+ compared with controls ($\beta = -1.10$ mm, FDR = 0.003) and PFX− ($\beta = -0.78$ mm, FDR = 0.042) as well as accelerated thinning compared with PFX− ($\beta = -0.074$ mm/year, FDR = 0.002). CC3, CC5, and CC6 ($\beta = -0.70$--0.48 mm, FDR = 0.002–0.022) showed significant thinning in PFX+ compared with controls. CC7 displayed significant thinning in PFX+ compared with both controls ($\beta = -1.36$ mm, FDR = 0.001) and PFX− ($\beta = -1.08$ mm, FDR = 0.006) (Table 2).

The analyses of the 30 putaminous segments showed thinning associated with aging most significantly in anterior putamen ((left segments 12–30, $t(127) = -5.93$--2.61, FDR <0.001–0.017; right segments 14–29, $t(127) = -3.48$--2.61, FDR = 0.003–0.017) and increased outer and inner distances in all segments except the most posterior segment (segments 2–30, $t(127) = 3.10$–8.01, FDR <0.001–0.002) (Fig. 3I, K). In addition, PFX+ exhibited significant thinning compared with controls most significantly in anterior putamen (left $t(84) = -3.33$--2.47, FDR = 0.01–0.049; right $t(84) = -4.01$--2.65, FDR <0.001–0.022) (Fig. 3E, F, J). Only segment 20 showed accelerated inner distance increase in PFX+ compared with controls ($t(124) = 3.38$, FDR = 0.001) (Fig. 3G, H, L).

3.4 VE at baseline predicts accelerated thinning in the CC and atrophy, thinning and distance increase in the putamen

The predictability analyses of baseline ventricular volume for subsequent structural changes revealed the associations of enlarged LV at baseline with accelerated CC thinning ($\beta = -0.0008$ mm/year, FDR = 0.010), left putamen atrophy ($\beta = -0.0004$ mm/year, FDR = 0.042), and increased putamen inner distance ($\beta = 0.0018$ mm/year, FDR = 0.042). V3 expansion at the baseline was associated with accelerated CC height increase ($\beta = 0.066$

mm/year, FDR = 0.010) and thinning ($\beta = -0.016$ mm/year, FDR = 0.025) as well as accelerated increases in putamen inner distance ($\beta = 0.050$ mm/year, FDR = 0.018) and outer distance ($\beta = 0.047$ mm/year, FDR = 0.027). Similarly, V4 expansion at the baseline was associated with accelerated CC height increase ($\beta = 0.064$ mm/year, FDR = 0.018), accelerated left putamen thinning ($\beta = -0.017$ mm/year, FDR = 0.017), and accelerated increase in inner distance ($\beta = 0.068$ mm/year, FDR = 0.007) (Table 3, Fig. 4A–D). These changes were all predicted using the mixed-effect model #3 (see section Statistical analysis) with only one interaction term: age by baseline value. Differential predictabilities in baseline ventricular volumes for accelerated changes among the groups were observed, but none of the three-way interactions were statistically significant.

3.5 Accelerated LV expansion is predicted by baseline values of CC thickness/height, putamen volume/distance, and V3 and V4 volumes

While none of the MRI measurements predicted changes in the V3 and V4, many baseline measurements were significantly associated with accelerated LV expansion, including CC height ($\beta = 0.18$ ml/year, FDR <0.001) and thickness ($\beta = -0.50$ ml/year, FDR = 0.010), and putamen volume (left/right $\beta = -0.79/-0.67$ ml/year, FDR = 0.021/0.042) and distance (inner & outer $\beta = 0.17$ ml/year, FDR = 0.007) (Fig. 4E, F). In addition, baseline volumes of V3 and V4 ventricles were also associated with accelerated LV expansion (v3/v4 $\beta = 1.18/0.61$ ml/year, FDR <0.001/0.007) (Table 3). Changes in the LV were predicted using the mixed-effects model #2 with both interaction terms of age-by-group and age-by-baseline value except for the prediction made by V3 that used model #3 with only one interaction term, age-by-baseline value. Fig. 4G summarizes the significant associations between baseline values and subsequent changes in MRI measurements.

3.6 VE and atrophy/deformation of the CC and putamen are associated with FXTAS progression and *FMR1* genetic markers

Changes in all MRI measurements showed significant associations with changes in FXTAS stage except CC length and putamen outer distance (Table 4). Changes in 11 measurements were also associated significantly with CGG repeat length. While ventricular volumes and putamen distance and volume showed quadratic relationships with CGG repeat length, CC height and thickness and putamen thickness showed linear relationships (Table 5, Fig. A.1 in the appendix). In addition, only right putamen volume showed a linear relationship with *FMR1* mRNA level ($\beta = -0.071$ ml, FDR = 0.044).

4. Discussion

In this longitudinal study, we examined the relationships between VE and structural changes in the CC (a periventricular white matter structure) and putamen (a non-periventricular subcortical gray matter structure) in males with *FMR1* normal and premutation alleles. All volumetric and morphologic MRI measurements except callosal length showed significant age-related changes common to all three groups (Table 2). In the comparisons of group mean and rate of change between the three groups, the only MRI measurement that showed differences in PFX− compared with controls was the significantly enlarged V4. In contrast, PFX+ showed a wide range of changes comprising: (1) enlarged V3 and V4 compared with

controls, and accelerated enlargement of the LV compared with both controls and PFX−; (2) callosal thinning compared with both controls and PFX−; and (3) putamen atrophy, thinning, and accelerated increase in inner distance compared with both controls and PFX− (Table 2, Fig. 2A–I). We further examined the predictabilities of baseline MRI measurements for changes in other brain regions. The results indicated that baseline enlargement in the V3 and V4 was associated with accelerated LV expansion, and baseline enlargement in all four ventricles was associated with morphological changes in the CC and putamen. In addition, baseline CC deformation and putamen atrophy and increased distance were associated with accelerated LV expansion, but not V3 or V4 expansion (Table 3, Fig. 4A–F). Changes in all MRI measurements except CC length and putamen outer distance showed significant associations with advances in FXTAS stage (Table 4). In addition, MRI measurements from all brain areas demonstrated significant associations with CGG repeat length in the premutation carriers, with ventricular volumes and putamen volume and inner distance showing quadratic relationships, and callosal height and thickness of the CC and putamen showing linear relationships (Table 5).

We have reported, in a cross-sectional study, significantly increased total ventricular volume in both PFX− and PFX+ relative to controls (Wang *et al.*, 2017). The current study extended the previous findings by indicating a potential temporal sequence of VE accompanying FXTAS progression. Since V4 was the only ventricle showing enlargement in PFX−, it appears to be the first ventricle affected by *FMR1* premutation. In contrast, LV, approximately 20-fold larger than V3 and V4, might be the last ventricles to be affected by FXTAS progression (Table 2). LV were the only ventricles exhibiting accelerated enlargement in PFX+ (without showing significant group differences), and the enlargement was revealed to be influenced broadly by baseline values of all structures-of-interest (Table 3, Fig. 4E–G). In addition, LV enlargement at baseline was associated with accelerated callosal thinning as well as accelerated distance increase and atrophy in the putamen (Table 3, Fig. 4A). The extensive interaction between LV enlargement and CC and putamen changes are consistent with the neuroanatomy of the LV, which are bordered by subcortical gray matter and white matter structures in all four lobes. Our study indicates that once VE has reached LV, a deleterious cycle between VE and brain structural deformation/atrophy can be formed, causing further VE and further brain structural deformation/atrophy (Fig. 4G).

As a major structure bordering the LV, the CC showed significant age-related atrophy, thinning, and height increase common for all groups. Interestingly, callosal atrophy was not a significant contributor to VE, contrary to the common understanding that the ventricles expand as a consequence of brain atrophy (Nestor *et al.*, 2008, Madsen *et al.*, 2015). Neither did baseline VE predict callosal atrophy. In contrast, CC thinning and height-increase showed significant interactions with VE (Table 3, Fig. 4A, B, E, G). These findings indicated that the CC may reorganize its structure by thinning and height-increase to accommodate VE, and individuals with CC morphological changes secondary to VE would experience further LV expansion. Our findings were concordant with those of a longitudinal study of mild cognitive impairment (MCI) and Alzheimer's disease (AD) to examine the link between baseline cortical atrophy and rate of ventricular expansion (Madsen *et al.*, 2015). Unexpectedly, baseline cortical thickness demonstrated more spatially extensive

correlation with LV expansion than cortical volume, and this relationship was statistically significant only in MCI, not in controls or in AD who exhibited the most brain atrophy and ventricular expansion amongst the three groups. Their findings disagreed with the assumption that brain atrophy was the only contributor to VE and warrant further investigations of VE as an important contributor to brain structural change in AD and other neurodegenerative diseases.

Interestingly, the non-periventricular subcortical gray matter structure, putamen, also showed changes inter-correlated significantly with VE in the three groups (Table 3, Fig. 4C, D, F, G), suggesting potential interactions between VE and structural changes in both periventricular and non-periventricular structures. As iron depositions in the putamen have been confirmed in a neuropathological examination (Ariza *et al.*, 2017), we are currently investigating the association of VE with iron depositions in the putamen, which may reveal pathogenic mechanism underlying iron depositions. The putamen encodes sensory and motor timing and sequences of actions and is critical for motor planning and reward-driven action selection (Herrero *et al.*, 2002, Paton and Buonomano, 2018). Lesions in the putamen have been associated with movement disorders such as dystonia and restless leg syndrome as well as cognitive deficits including apathy and disinhibition (Bhatia and Marsden, 1994, Park, 2016). Higher rates of apathy (39.5% of male PFX+) (Grigsby *et al.*, 2016) and restless leg syndrome (33.1% in male and female carriers) (Summers *et al.*, 2014) compared with controls have been reported, and dystonia has been observed in 11% of the carriers (Vaughan *et al.*, 2012). These findings point to a potential link between putamen and clinical symptoms of FXTAS. Investigate are needed for the associations between VE, iron depositions in the putamen, and motor/cognitive deficits in FXTAS.

To further characterize VE, we followed the international guidelines of CT or MRI signs for NPH diagnosis and selection of shunt-responsive patients, comprising Evans index (>0.3) and CC angle (<90°) (Ishii *et al.*, 2008, Damasceno, 2015). NPH is a form of CSF circulation disorder in older people with neurological symptoms overlapping with FXTAS, namely gait disturbance, urinary incontinence, and dementia (Pena *et al.*, 2002, Keong *et al.*, 2016). While 19/39 PFX+, 2 PFX−, and 3 controls met the Evans index criterion, only 3 PFX+, 1 PFX−, and 1 control met both criteria for NPH (Table 1). All four carriers who met the NPH criteria had gait disturbance and urinary incontinence/urgency whereas the control who met the criteria did not. Currently, the primary treatment for NPH is through surgical intervention, such as ventricular shunting and/or endoscopic third ventriculostomy. Although these procedures could reverse brain structural damage associated with NPH, both are invasive and can lead to serious complications (Di Curzio, 2018). Premutation carriers are vulnerable to environmental toxins and may not be the ideal candidates for these invasive procedures as prolonged general anesthesia may trigger early onset of FXTAS or worsen their neurological symptoms (Polussa *et al.*, 2014, Ligsay *et al.*, 2018).

Understanding pathophysiological underpinning of VE is important because it offers novel targets for therapeutic treatments. In line with our findings, frequent intranuclear inclusions, the pathological hallmark of FXTAS, have been detected in the ependymal cells for ventricular lining and epithelial lining cells of the choroid plexus, signaling cellular distress (Tassone *et al.*, 2004). These cells are vital for CSF production and circulation as

dysfunction may lead to imbalanced CSF production and absorption and ventricular enlargement (Silverberg *et al.*, 2003, Simon and Iliff, 2016). Future studies exploring pathophysiologic mechanisms of VE in FXTAS could calibrate CSF circulation using *in vivo* MRI enhanced with an intrathecal contrast agent as a CSF tracer. Such studies have been performed, which demonstrated a delayed CSF clearance in patients with NPH (Eide *et al.*, 2018, Ringstad *et al.*, 2018). Mouse models of *FMR1* premutation can also be used to investigate the relationships between CSF circulation and production and the formation of intranuclear inclusions in the ependymal ventricular lining cells and epithelial choroidal cells.

Limitations of the study include the fact that patients were not followed for all stages of FXTAS. PFX+ were significantly older compared with both controls and PFX−, which might have impacted the results regarding PFX+ even after including age as a covariate in all mixed-effects models. The potential impact could be great variation for older PFX+ that would lead to lack of statistical power for detecting a significant difference given a relatively small sample size. In addition, factors leading to VE (e.g., CSF production, absorption, and circulation, atrophy in other brain areas, etc.), and how changes in microstructural integrity (measured using diffusion MRI) in the CC and other periventricular white matter structures affect the relationships between VE and atrophy/deformation remain to be explored.

5. Conclusions

We demonstrated a progressive ventricular expansion from V4 to V3 and LV that may be associated with accelerated deformation in the CC and putamen as well as a deleterious cycle between progressive ventricular expansion and progressive deformation and/or atrophy in the CC and putamen in males with *FMR1* normal and premutation alleles during aging. In premutation carriers, these processes were accelerated, with expanded CGG-repeats in the premutation range being an apparent driving factor. Our study indicates the potential of ventricular expansion as an important mechanical mechanism contributing to neurodegeneration common for both aging and neurodegenerative disorders.

Supplementary Material

Refer to Web version on PubMed Central for supplementary material.

Acknowledgments

Abbreviations:

CC   corpus callosum

CSF	cerebrospinal fluid
FDR	false discovery rate
FXTAS	fragile X-associated tremor/ataxia syndrome
LV	lateral ventricles
NPH	normal pressure hydrocephalus
PFX−	premutation carriers without FXTAS
PFX+	premutation carriers with FXTAS
T1V	time one variable
V3	third ventricle
V4	fourth ventricle
VE	ventricular expansion

References

Acosta-Cabronero J, Williams GB, Cardenas-Blanco A, Arnold RJ, Lupson V, Nestor PJ. In vivo quantitative susceptibility mapping (QSM) in Alzheimer's disease. PLoS One 2013; 8: e81093. [PubMed: 24278382]

Albeck MJ, Skak C, Nielsen PR, Olsen KS, Borgesen SE, Gjerris F. Age dependency of resistance to cerebrospinal fluid outflow. J Neurosurg 1998; 89: 275–8. [PubMed: 9688123]

Apostolova LG, Green AE, Babakchanian S, Hwang KS, Chou YY, Toga AW, Thompson PM. Hippocampal atrophy and ventricular enlargement in normal aging, mild cognitive impairment (MCI), and Alzheimer Disease. Alzheimer Dis Assoc Disord 2012; 26: 17–27. [PubMed: 22343374]

Ariza J, Rogers H, Hartvigsen A, Snell M, Dill M, Judd D, Hagerman P, Martinez-Cerdeno V. Iron accumulation and dysregulation in the putamen in fragile X-associated tremor/ataxia syndrome. Mov Disord 2017; 32: 585–91. [PubMed: 28233916]

Bacalman S, Farzin F, Bourgeois JA, Cogswell J, Goodlin-Jones BL, Gane LW, Grigsby J, Leehey MA, Tassone F, Hagerman RJ. Psychiatric phenotype of the fragile X-associated tremor/ataxia syndrome (FXTAS) in males: newly described fronto-subcortical dementia. J Clin Psychiatry 2006; 67: 87–94. [PubMed: 16426093]

Bakdash JZ, Marusich LR. Repeated Measures Correlation. Front Psychol 2017; 8: 456. [PubMed: 28439244]

Battistella G, Niederhauser J, Fornari E, Hippolyte L, Gronchi Perrin A, Lesca G, Forzano F, Hagmann P, Vingerhoets FJ, Draganski B, Maeder P, Jacquemont S. Brain structure in asymptomatic FMR1 premutation carriers at risk for fragile X-associated tremor/ataxia syndrome. Neurobiol Aging 2013; 34: 1700–7. [PubMed: 23298734]

Benjamini Y, Hochberg Y. Controlling the False Discovery Rate - a Practical and Powerful Approach to Multiple Testing. J R Statist Soc B 1995; 57: 289–300.

Bhatia KP, Marsden CD. The behavioural and motor consequences of focal lesions of the basal ganglia in man. Brain 1994; 117 (Pt 4): 859–76. [PubMed: 7922471]

Brunberg JA, Jacquemont S, Hagerman RJ, Berry-Kravis EM, Grigsby J, Leehey MA, Tassone F, Brown WT, Greco CM, Hagerman PJ. Fragile X premutation carriers: characteristic MR imaging findings of adult male patients with progressive cerebellar and cognitive dysfunction. AJNR Am J Neuroradiol 2002; 23: 1757–66. [PubMed: 12427636]

Buckner RL, Head D, Parker J, Fotenos AF, Marcus D, Morris JC, Snyder AZ. A unified approach for morphometric and functional data analysis in young, old, and demented adults using automated atlas-based head size normalization: reliability and validation against manual measurement of total intracranial volume. Neuroimage 2004; 23: 724–38. [PubMed: 15488422]

Cherubini A, Peran P, Caltagirone C, Sabatini U, Spalletta G. Aging of subcortical nuclei: microstructural, mineralization and atrophy modifications measured in vivo using MRI. Neuroimage 2009; 48: 29–36. [PubMed: 19540925]

Cohen S, Masyn K, Adams J, Hessl D, Rivera S, Tassone F, Brunberg J, DeCarli C, Zhang L, Cogswell J, Loesch D, Leehey M, Grigsby J, Hagerman PJ, Hagerman R. Molecular and imaging correlates of the fragile X-associated tremor/ataxia syndrome. Neurology 2006; 67: 1426–31. [PubMed: 17060569]

Damasceno BP. Neuroimaging in normal pressure hydrocephalus. Dement Neuropsychol 2015; 9: 350–5. [PubMed: 29213984]

de Jong LW, van der Hiele K, Veer IM, Houwing JJ, Westendorp RG, Bollen EL, de Bruin PW, Middelkoop HA, van Buchem MA, van der Grond J. Strongly reduced volumes of putamen and thalamus in Alzheimer's disease: an MRI study. Brain 2008; 131: 3277–85. [PubMed: 19022861]

Di Curzio DL. Neuropathological changes in hydrocephalus-A comprehensive review. Open Journal of Modern Neurosurgery 2018; 8: 1–29.

Eide PK, Vatnehol SAS, Emblem KE, Ringstad G. Magnetic resonance imaging provides evidence of glymphatic drainage from human brain to cervical lymph nodes. Sci Rep 2018; 8: 7194. [PubMed: 29740121]

Filipovic-Sadic S, Sah S, Chen L, Krosting J, Sekinger E, Zhang W, Hagerman PJ, Stenzel TT, Hadd AG, Latham GJ, Tassone F. A novel FMR1 PCR method for the routine detection of low abundance expanded alleles and full mutations in fragile X syndrome. Clin Chem 2010; 56: 399–408. [PubMed: 20056738]

Fujii S, Matsusue E, Kinoshita T, Sugihara S, Ohama E, Ogawa T. Hyperintense putaminal rim at 3T reflects fewer ferritin deposits in the lateral marginal area of the putamen. AJNR Am J Neuroradiol 2007; 28: 777–81. [PubMed: 17416838]

Grigsby J, Brega AG, Bennett RE, Bourgeois JA, Seritan AL, Goodrich GK, Hagerman RJ. Clinically significant psychiatric symptoms among male carriers of the fragile X premutation, with and without FXTAS, and the mediating influence of executive functioning. Clin Neuropsychol 2016; 30: 944–59. [PubMed: 27355103]

Hagerman PJ, Hagerman RJ. Fragile X-associated tremor/ataxia syndrome. Annals of the New York Academy of Sciences 2015; 1338: 58–70. [PubMed: 25622649]

Hagerman R, Hagerman P. Advances in clinical and molecular understanding of the FMR1 premutation and fragile X-associated tremor/ataxia syndrome. Lancet neurology 2013; 12: 786–98. [PubMed: 23867198]

Hagerman RJ, Hall DA, Coffey S, Leehey M, Bourgeois J, Gould J, Zhang L, Seritan A, Berry-Kravis E, Olichney J, Miller JW, Fong AL, Carpenter R, Bodine C, Gane LW, Rainin E, Hagerman H, Hagerman PJ. Treatment of fragile X-associated tremor ataxia syndrome (FXTAS) and related neurological problems. Clin Interv Aging 2008; 3: 251–62. [PubMed: 18686748]

Hagerman RJ, Leehey M, Heinrichs W, Tassone F, Wilson R, Hills J, Grigsby J, Gage B, Hagerman PJ. Intention tremor, parkinsonism, and generalized brain atrophy in male carriers of fragile X. Neurology 2001; 57: 127–30. [PubMed: 11445641]

Hakim S, Adams RD. The special clinical problem of symptomatic hydrocephalus with normal cerebrospinal fluid pressure. Observations on cerebrospinal fluid hydrodynamics. J Neurol Sci 1965; 2: 307–27. [PubMed: 5889177]

Hashimoto R, Javan AK, Tassone F, Hagerman RJ, Rivera SM. A voxel-based morphometry study of grey matter loss in fragile X-associated tremor/ataxia syndrome. Brain 2011; 134: 863–78. [PubMed: 21354978]

Herrero MT, Barcia C, Navarro JM. Functional anatomy of thalamus and basal ganglia. Childs Nerv Syst 2002; 18: 386–404. [PubMed: 12192499]

Ishii K, Kanda T, Harada A, Miyamoto N, Kawaguchi T, Shimada K, Ohkawa S, Uemura T, Yoshikawa T, Mori E. Clinical impact of the callosal angle in the diagnosis of idiopathic normal pressure hydrocephalus. Eur Radiol 2008; 18: 2678–83. [PubMed: 18500524]

Keong NC, Pena A, Price SJ, Czosnyka M, Czosnyka Z, Pickard JD. Imaging normal pressure hydrocephalus: theories, techniques, and challenges. Neurosurg Focus 2016; 41: E11.

Levine DN. Intracranial pressure and ventricular expansion in hydrocephalus: have we been asking the wrong question? J Neurol Sci 2008; 269: 1–11. [PubMed: 18234229]

Ligsay A, El-Deeb M, Salcedo-Arellano MJ, Schloemerkemper N, Grayson JS, Hagerman R. General Anesthetic Use in Fragile X Spectrum Disorders. J Neurosurg Anesthesiol 2018.

Linninger AA, Tsakiris C, Zhu DC, Xenos M, Roycewicz P, Danziger Z, Penn R. Pulsatile cerebrospinal fluid dynamics in the human brain. IEEE Trans Biomed Eng 2005; 52: 557–65. [PubMed: 15825857]

Madsen SK, Gutman BA, Joshi SH, Toga AW, Jack CR, Jr., Weiner MW, Thompson PM, Alzheimer's Disease Neuroimaging I. Mapping ventricular expansion onto cortical gray matter in older adults. Neurobiol Aging 2015; 36 Suppl 1: S32–41. [PubMed: 25311280]

Nestor SM, Rupsingh R, Borrie M, Smith M, Accomazzi V, Wells JL, Fogarty J, Bartha R, Alzheimer's Disease Neuroimaging I. Ventricular enlargement as a possible measure of Alzheimer's disease progression validated using the Alzheimer's disease neuroimaging initiative database. Brain 2008; 131: 2443–54. [PubMed: 18669512]

Park J. Movement Disorders Following Cerebrovascular Lesion in the Basal Ganglia Circuit. J Mov Disord 2016; 9: 71–9. [PubMed: 27240808]

Paton JJ, Buonomano DV. The Neural Basis of Timing: Distributed Mechanisms for Diverse Functions. Neuron 2018; 98: 687–705. [PubMed: 29772201]

Pena A, Harris NG, Bolton MD, Czosnyka M, Pickard JD. Communicating hydrocephalus: the biomechanics of progressive ventricular enlargement revisited. Acta Neurochir Suppl 2002; 81: 59–63. [PubMed: 12168357]

Polussa J, Schneider A, Hagerman R. Molecular Advances Leading to Treatment Implications for Fragile X Premutation Carriers. Brain disorders & therapy 2014; 3.

Ringstad G, Valnes LM, Dale AM, Pripp AH, Vatnehol SS, Emblem KE, Mardal KA, Eide PK. Brain-wide glymphatic enhancement and clearance in humans assessed with MRI. JCI Insight 2018; 3.

Satow T, Aso T, Nishida S, Komuro T, Ueno T, Oishi N, Nakagami Y, Odagiri M, Kikuchi T, Yoshida K, Ueda K, Kunieda T, Murai T, Miyamoto S, Fukuyama H. Alteration of Venous Drainage Route in Idiopathic Normal Pressure Hydrocephalus and Normal Aging. Front Aging Neurosci 2017; 9: 387. [PubMed: 29218007]

Silverberg GD, Mayo M, Saul T, Rubenstein E, McGuire D. Alzheimer's disease, normal-pressure hydrocephalus, and senescent changes in CSF circulatory physiology: a hypothesis. Lancet neurology 2003; 2: 506–11. [PubMed: 12878439]

Simon MJ, Iliff JJ. Regulation of cerebrospinal fluid (CSF) flow in neurodegenerative, neurovascular and neuroinflammatory disease. Biochim Biophys Acta 2016; 1862: 442–51. [PubMed: 26499397]

Smith SM. Fast robust automated brain extraction. Hum Brain Mapp 2002; 17: 143–55. [PubMed: 12391568]

Smith SM, Jenkinson M, Woolrich MW, Beckmann CF, Behrens TE, Johansen-Berg H, Bannister PR, De Luca M, Drobnjak I, Flitney DE, Niazy RK, Saunders J, Vickers J, Zhang Y, De Stefano N, Brady JM, Matthews PM. Advances in functional and structural MR image analysis and implementation as FSL. Neuroimage 2004; 23 Suppl 1: S208–19. [PubMed: 15501092]

Smith SM, Zhang Y, Jenkinson M, Chen J, Matthews PM, Federico A, De Stefano N. Accurate, robust, and automated longitudinal and cross-sectional brain change analysis. Neuroimage 2002; 17: 479–89. [PubMed: 12482100]

Summers SM, Cogswell J, Goodrich JE, Mu Y, Nguyen DV, Brass SD, Hagerman RJ. Prevalence of restless legs syndrome and sleep quality in carriers of the fragile X premutation. Clin Genet 2014; 86: 181–4. [PubMed: 25180401]

Tang X, Oishi K, Faria AV, Hillis AE, Albert MS, Mori S, Miller MI. Bayesian Parameter Estimation and Segmentation in the Multi-Atlas Random Orbit Model. PLoS One 2013; 8: e65591. [PubMed: 23824159]

Tassone F, Hagerman RJ, Garcia-Arocena D, Khandjian EW, Greco CM, Hagerman PJ. Intranuclear inclusions in neural cells with premutation alleles in fragile X associated tremor/ataxia syndrome. J Med Genet 2004; 41: e43. [PubMed: 15060119]

Tassone F, Hagerman RJ, Taylor AK, Gane LW, Godfrey TE, Hagerman PJ. Elevated levels of FMR1 mRNA in carrier males: a new mechanism of involvement in the fragile-X syndrome. Am J Hum Genet 2000; 66: 6–15. [PubMed: 10631132]

Tassone F, Pan R, Amiri K, Taylor AK, Hagerman PJ. A rapid polymerase chain reaction-based screening method for identification of all expanded alleles of the fragile X (FMR1) gene in newborn and high-risk populations. J Mol Diagn 2008; 10: 43–9. [PubMed: 18165273]

Tustison NJ, Avants BB, Cook PA, Zheng Y, Egan A, Yushkevich PA, Gee JC. N4ITK: improved N3 bias correction. IEEE transactions on medical imaging 2010; 29: 1310–20. [PubMed: 20378467]

Vaughan C, Ouyang B, Goetz C, Berry-Kravis E, Hagerman R, Leehey M, Hall D. Dystonia in FMR1 premutation carriers. Neurology 2012; 78 (Meeting Abstracts 1:P01.222-P01.222).

Wang H, Das SR, Suh JW, Altinay M, Pluta J, Craige C, Avants B, Yushkevich PA, Alzheimer's Disease Neuroimaging I. A learning-based wrapper method to correct systematic errors in automatic image segmentation: consistently improved performance in hippocampus, cortex and brain segmentation. Neuroimage 2011; 55: 968–85. [PubMed: 21237273]

Wang H, Pouch A, Takabe M, Jackson B, Gorman J, Gorman R, Yushkevich PA. Multi-atlas segmentation with robust label transfer and label fusion. Information processing in medical imaging : proceedings of the conference 2013a; 23: 548–59. [PubMed: 24683998]

Wang JY, Hagerman RJ, Rivera SM. A multimodal imaging analysis of subcortical gray matter in fragile X premutation carriers. Mov Disord 2013b; 28: 1278–84. [PubMed: 23649693]

Wang JY, Hessl D, Hagerman RJ, Simon TJ, Tassone F, Ferrer E, Rivera SM. Abnormal trajectories in cerebellum and brainstem volumes in carriers of the fragile X premutation. Neurobiol Aging 2017; 55: 11–9. [PubMed: 28391068]

Wang JY, Hessl DH, Hagerman RJ, Tassone F, Rivera SM. Age-dependent structural connectivity effects in fragile x premutation. Arch Neurol 2012; 69: 482–9. [PubMed: 22491193]

Wang JY, Ngo MM, Hessl D, Hagerman RJ, Rivera SM. Robust Machine Learning-Based Correction on Automatic Segmentation of the Cerebellum and Brainstem. PLoS One 2016; 11: e0156123. [PubMed: 27213683]

Weis S, Kimbacher M, Wenger E, Neuhold A. Morphometric analysis of the corpus callosum using MR: correlation of measurements with aging in healthy individuals. AJNR Am J Neuroradiol 1993; 14: 637–45. [PubMed: 8517352]

Witelson SF. Hand and sex differences in the isthmus and genu of the human corpus callosum. A postmortem morphological study. Brain 1989; 112 (Pt 3): 799–835. [PubMed: 2731030]

Yushkevich PA, Piven J, Hazlett HC, Smith RG, Ho S, Gee JC, Gerig G. User-guided 3D active contour segmentation of anatomical structures: significantly improved efficiency and reliability. Neuroimage 2006; 31: 1116–28. [PubMed: 16545965]

Highlights

- Significant age-related callosal and putamen deformation and VE in all groups.

- Progressive VE from V4 to V3 and LV in *FMR1* premutation carriers.

- Baseline VE predicted accelerated deformation of the corpus callosum and putamen.

- Baseline callosal and putamen deformation predicted accelerated LV expansion.
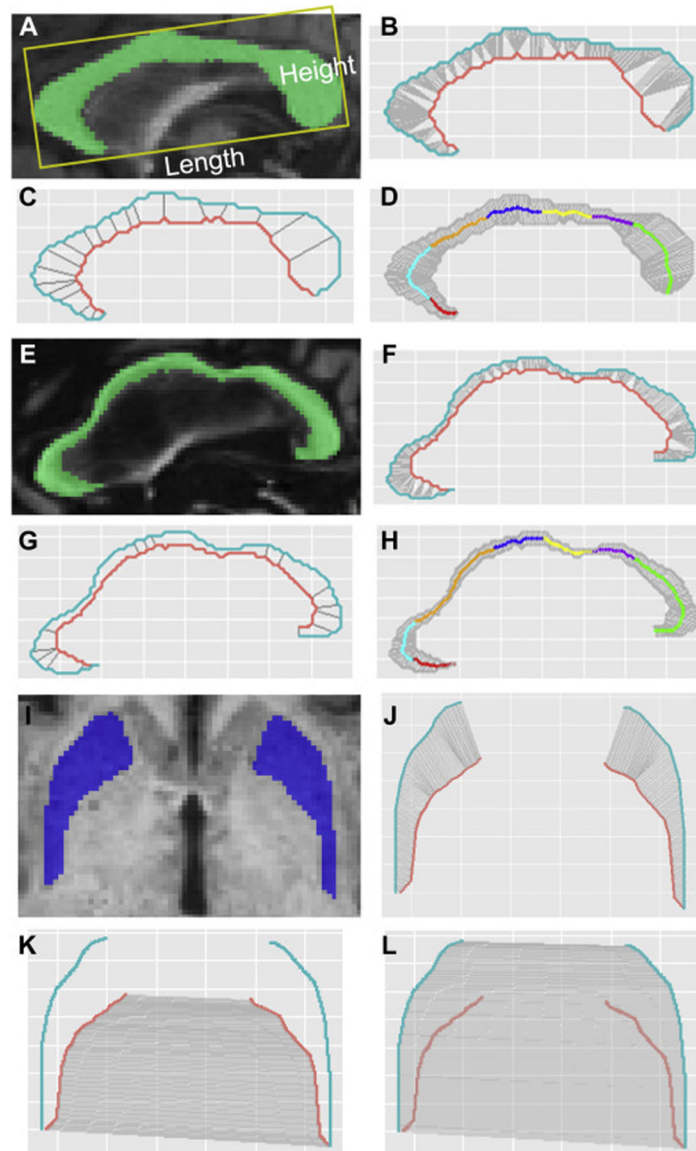
Fig. 1. Morphological measurements of the CC and putamen.
(A-D) A 63-year-old patient at FXTAS stage 2 without substantial morphological changes in the CC. (E-H) A 78-year-old patient at FXTAS stage 3 with substantial morphological changes in the CC. (A) CC length and height. (A, E) CC segmentation. (B, F) The determination of inflection points on the lower boundary (orange curve). (C, G) CC sections (gray straight lines). (D, H) 300 CC segments and anatomic subregions determined using Witelson's method (Witelson, 1989): red, the rostrum (CC1); cyan, genu (CC2); orange, rostral body (CC3); blue, anterior midbody (CC4); yellow, posterior midbody (CC5); purple, isthmus (CC6); and green, splenium (CC7). (I) Segmentation of the putamen. (J) 150 segments of the putamen. (K) The calculation of putamen inner distance using the 150 gray lines linking the corresponding points on the inner boundaries (orange) of the left and right putamen. (L) The calculation of putamen outer distance using the 150 gray lines linking the corresponding points on the outer boundaries (blue) of the left and right putamen.

Fig. 2. Longitudinal changes in MRI measurements.
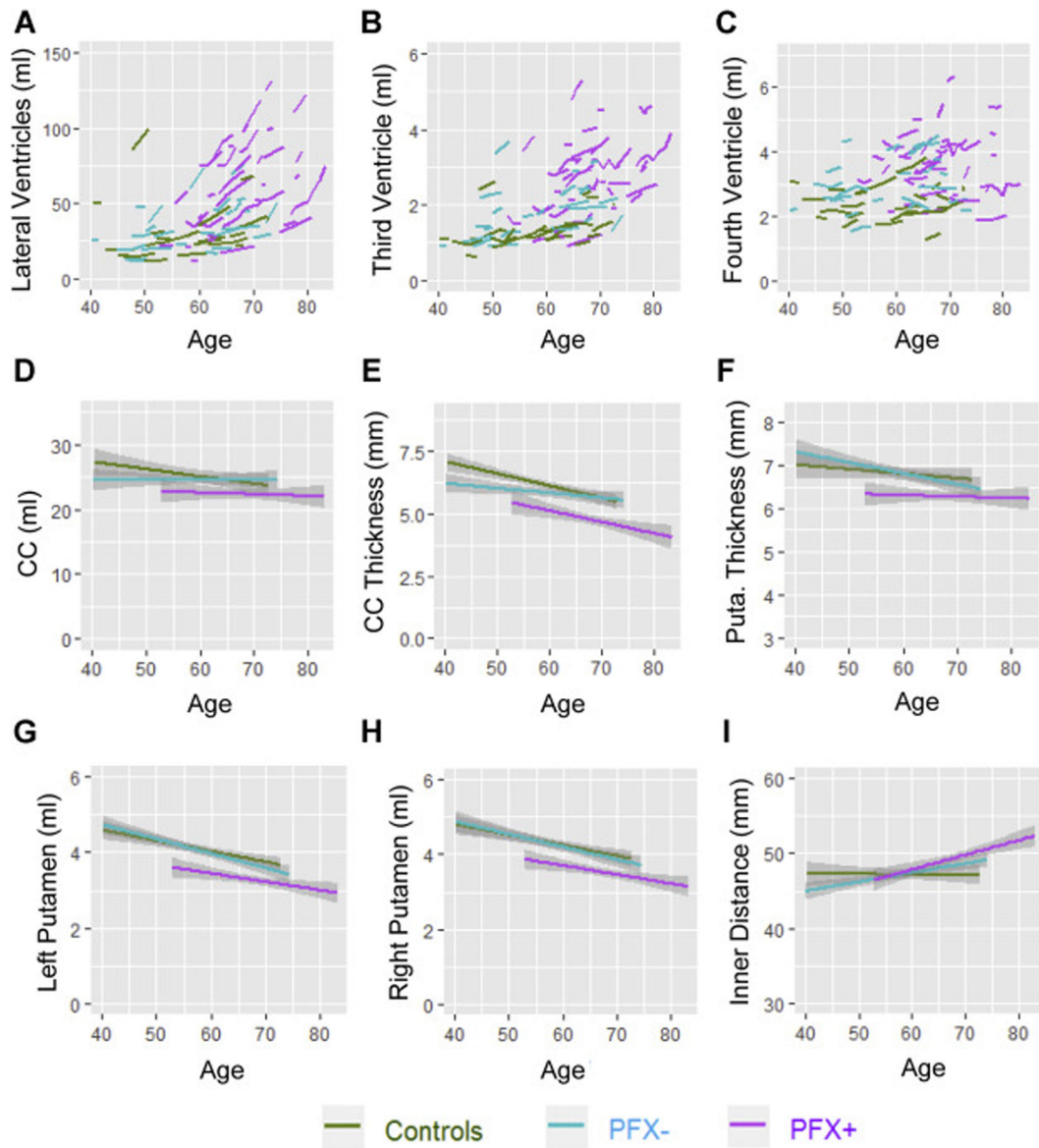(A) Longitudinal changes in LV volume. (B) Longitudinal changes in V3 volume. (C) Longitudinal changes in V4 volume. (D) Longitudinal changes in CC volume. (E) Longitudinal changes in CC thickness. (F) Longitudinal changes in right putamen thickness. (G, H) Longitudinal changes in left and right putamen volumes. (I) Longitudinal changes in putamen inner distance.
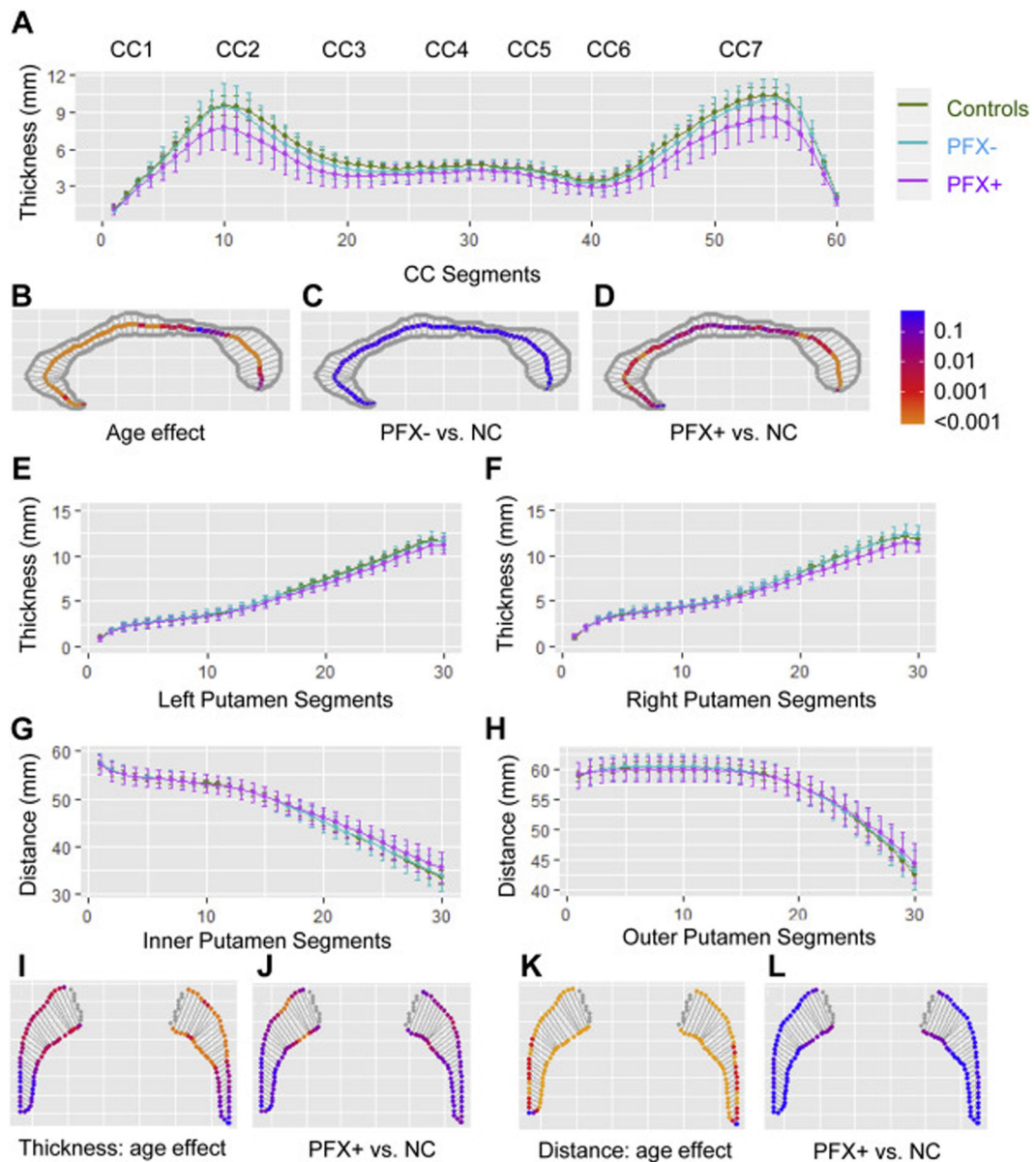
Fig. 3. The results of mixed-effects models for the callosal and putamen segments.
(A) The coefficients and their 95% confidence interval for the thickness of the 60 CC segments. (B) The age effect on the thickness of 60 CC segments for all three groups. (C) The comparisons of the CC segments between PFX− and controls. (D) The comparisons of the CC segments between PFX+ and controls. (E, F) The coefficients and their 95% confidence interval for the thickness of the 30 left and right putamen segments. (G, H) The coefficients and their 95% confidence interval for putamen inner and outer distances of the 30 segments. (I) The age effect on the thickness of left and right putamen common for all three groups. (J) The comparisons of putamen thickness between PFX+ and controls. (K) The age effect on the distance of left and right putamen common for all three groups. (L) The comparisons of putamen distance between PFX+ and controls. Multiple comparison-corrected *p* values are shown in C-D & I-L.
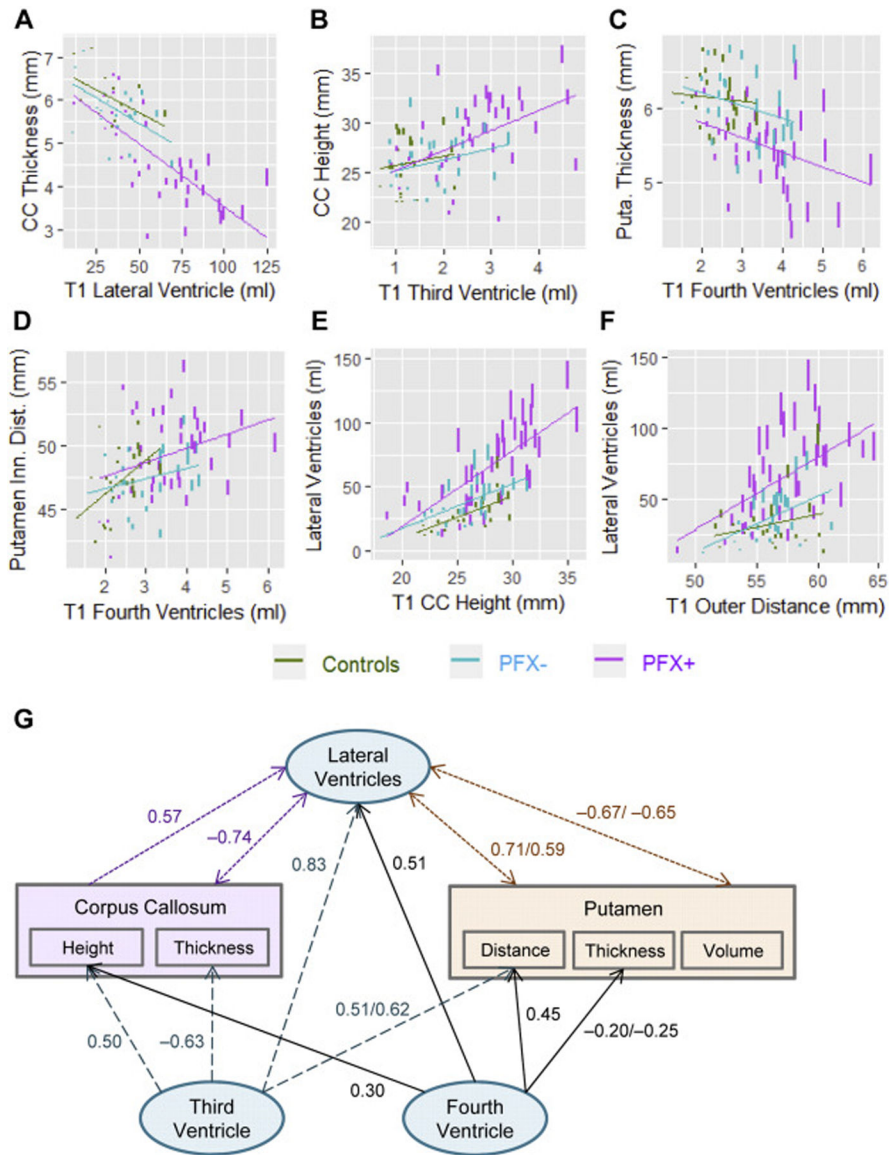
Fig. 4. Predictions of longitudinal changes using baseline (T1) measures.
(A) Baseline LV volume and changes in CC thickness. (B) Baseline V3 volume and changes in CC height. (C) Baseline V4 volume and changes in the thickness of left putamen. (D) Baseline V4 volume and changes in putamen inner distance. (E) Baseline CC height and changes in LV volume. (F) Baseline putamen outer distance and changes in LV volume. The y-axes show the fitted values estimated by mix-effects models. Vertical lines in the plots indicate the predicted amount of changes five years after the time 1 visits. Regression lines show the slope for each group between the baseline and the fitted variable. (G) The model of inter-correlations between ventricular expansion and structural changes in the CC and putamen. Blue dash lines show changes predicted by baseline V3 enlargement while black solid lines depict changes predicted by baseline V4 enlargement, purple dotted line depict changes predicted by baseline CC height increase, purple dotted line show changes predicted by baseline LV enlargement, and orange dotted lines show changes predicted by baseline

putamen measurements. Numbers indicate repeated-measures correlations between predicting and predicted variables, calculated using the R Package 'rmcorr' (Bakdash and Marusich, 2017).

Table 1.

Characteristics of research participants: Mean (SD) [Range]

	Controls (*N* = 22)	PFX– (*N* = 26)	PFX+ (*N* = 39)
Age at T1 (year)	56.6 (9.4) [40–72]	57.7 (9.0) [40–72]	66.3 (6.5) [52–77]
Number of visits	2.5 (0.51) [2–3]	2.3 (0.55) [2–4]	2.6 (1.1) [2–7]
2 visits (*N*)	12	19	25
3 visits (*N*)	10	6	10
4 visits (*N*)	0	1	2
5 visits (*N*)	0	0	0
6 visits (*N*)	0	0	1
7 visits (*N*)	0	0	1
Years between visits	2.6 (0.88) [0.2–4.8]	2.2 (1.31) [0.28–7.3]	1.6 (0.97) [0.3–5.1]
Years elapsed between first and last visits	3.7 (2.0) [0.2–7.5]	2.9 (1.6) [1.1–7.3]	2.6 (1.8) [0.8–7.1]
Evans index at T1	0.26 (0.03) [0.22–0.35]	0.26 (0.011) [0.19–0.34]	0.29 (0.05) [0.17–0.39]
CC angle at T1	114.0 (15.32) [70–136]	111.5 (14.5) [72–136]	111.3 (14.3) [82–136]
Evans index >0.3 (*N*)	3	2	19
CC angle <90° (*N*)	1	2	4
Meet criteria for NPH (*N*)	1	1	3
FMR1 CGG repeat size	28.2 (6.0) [19–42]	80.5 (17.2) [59–113]	96.5 (20.9) [62–154]
FMR1 mRNA at T1 [*]	1.22 (0.21) [0.9–1.59]	2.37 (0.67) [1.23–4.03]	2.58 (0.63) [1.67–4.5]

[*] $N_{Control}$ = 20, $N_{PFX–}$ = 25, N_{PFX+} = 37

Table 2.

Group differences in longitudinal changes in MRI measurements

Brain Areas	N	All Groups	PFX− Vs. NC		PFX+ Vs. NC		PFX+ Vs. PFX−	
		β_{age} (SE)	β_{Group} (SE)	$\beta_{Group \times Age}$ [#] (SE)	β_{Group} (SE)	$\beta_{Group \times Age}$ [#] (SE)	β_{Group} (SE)	$\beta_{Group \times Age}$ [#] (SE)
Ventricles								
Lateral (ml)	87	**0.81 (0.27)**	3.45 (6.43)	0.42 (0.38)	10.4 (5.93)	**2.03 (0.36)**	6.92 (5.62)	**1.61 (0.36)**
Third (ml)	87	**0.045 (0.004)**	0.39 (0.19)	-	**0.68 (0.19)**	-	0.29 (0.18)	-
Fourth (ml)	87	**0.029 (0.005)**	**0.64 (0.21)**	-	**0.92 (0.21)**	-	0.28 (0.20)	-
Corpus callosum								
Volume (ml)	86	**−0.102 (0.017)**	−0.49 (0.94)	-	−1.69 (0.88)	-	−1.20 (0.83)	-
Length (mm)	86	−0.011 (0.023)	−0.18 (1.65)	-	−0.50 (1.50)	-	−0.32 (1.43)	-
Height (mm)	86	**0.119 (0.019)**	−0.59 (0.99)	-	0.49 (0.95)	-	1.08 (0.90)	-
Thickness (mm)	86	**−0.057 (0.006)**	−0.30 (0.25)	-	**−0.90 (0.23)**	-	**−0.60 (0.22)**	-
CC1 thickness (mm)	86	**−0.018 (0.006)**	−0.32 (0.14)	-	−0.29 (0.14)	-	−0.03 (0.13)	-
CC2 thickness (mm)	86	**−0.051 (0.016)**	−0.32 (0.34)	0.023 (0.024)	**−1.10 (0.33)**	−0.051 (0.022)	**−0.78 (0.31)**	**−0.074 (0.023)**
CC3 thickness (mm)	86	**−0.050 (0.006)**	−0.34 (0.21)	-	**−0.70 (0.20)**	-	−0.36 (0.19)	-
CC4 thickness (mm)	86	**−0.037 (0.007)**	−0.22 (0.20)	-	−0.39 (0.19)	-	−0.18 (0.18)	-
CC5 thickness (mm)	86	**−0.030 (0.007)**	−0.18 (0.21)	-	**−0.48 (0.20)**	-	−0.30 (0.19)	-
CC6 thickness (mm)	86	**−0.035 (0.008)**	−0.16 (0.27)	-	**−0.66 (0.26)**	-	−0.50 (0.24)	-
CC7 thickness (mm)	86	**−0.064 (0.010)**	−0.28 (0.36)	-	**−1.36 (0.35)**	-	**−1.08 (0.32)**	-
Putamen								
Left (ml)	87	**−0.042 (0.004)**	−0.039 (0.14)	-	**−0.45 (0.13)**	-	**−0.42 (0.12)**	-
Right (ml)	87	**−0.032 (0.006)**	−0.050 (0.14)	−0.009 (0.009)	**−0.41 (0.14)**	−0.018 (0.009)	**−0.36 (0.13)**	−0.010 (0.009)
Thickness left (mm)	87	**−0.030 (0.005)**	−0.016 (0.12)	-	−0.30 (0.13)	-	−0.28 (0.12)	-
Thickness right (mm)	87	**−0.023 (0.006)**	0.010 (0.14)	-	**−0.39 (0.14)**	-	**−0.40 (0.13)**	-
Inner distance (mm)	87	**0.089 (0.019)**	0.102 (0.63)	0.006 (0.043)	0.130 (0.63)	**0.126 (0.042)**	0.028 (0.57)	**0.120 (0.043)**
Outer distance (mm)	87	**0.11 (0.030)**	0.046 (0.63)	-	−0.091 (0.61)	-	−0.14 (0.58)	-

[#] When age by group interaction was included in the model. All comparisons in the bold font passed both Bonferroni correction for multiple group comparisons and FDR correction for all hypotheses tested in one type of analysis. Regional CC thickness comparisons for CC1 to CC7 were performed as post-hoc analyses. Models predicting volumes used brain scaling factor as a covariate while models predicting length, height, thickness, and distance used inner skull width as a covariate.

Table 3.

Associations of baseline MRI data with accelerated changes in the three groups

MRI Measurements	N	β	SE	FDR	Model #[*]
Changes predicted by baseline lateral ventricular volume (ml)					
Corpus callosum					
Thickness (mm/year)	86	−0.0007	0.0003	0.010	3
Putamen					
Volume left (ml/year)	87	−0.0004	0.0002	0.042	3
Inner distance (mm/year)	87	0.0018	0.0007	0.042	3
Changes predicted by baseline third ventricular volume (ml)					
Lateral ventricles (ml/year)	87	1.18	0.14	<0.001	3
Corpus callosum					
Height (mm/year)	86	0.066	0.021	0.010	3
Thickness (mm/year)	86	−0.016	0.006 *J*	0.025	3
Putamen					
Inner distance (mm/year)	87	0.050	0.0170	0.018	3
Outer distance (mm/year)	87	0.047	0.0175	0.027	3
Changes predicted by baseline fourth ventricular volume (ml)					
Lateral ventricles (ml/year)	87	0.61	0.180	0.007	2
Corpus callosum					
Height (mm/year)	86	0.064	0.022	0.018	3
Putamen					
Thickness left (mm/year)	87	−0.017	0.006	0.017	3
Inner distance (mm/year)	87	0.068	0.020	0.007	3
Predicting changes in lateral ventricles (ml/year)					
Corpus callosum					
Height (mm)	86	0.18	0.039	<0.001	2
Thickness (mm)	86	−0.50	0.16	0.010	2
Putamen					
Volume left (ml)	87	−0.79	0.28	0.021	2
Volume right (ml)	87	−0.67	0.27	0.042	2
Inner distance (mm)	87	0.17	0.05	0.007	2
Outer distance (mm)	87	0.17	0.05	0.007	2

[*] Corresponds to the nested mixed-effects models chosen as a final model determined by likelihood ratio test (see Statistical analysis section for details). Since at least one volume variable was present in each model, brain scaling factor was used as a covariate in all of the models.

Table 4.

Associations between longitudinal MRI measurements and FXTAS stage in premutation carriers ($N = 65$)

MRI Measurements	β	SE	FDR
Ventricles			
LV (ml)	0.026	0.005	**<0.001**
V3 (ml)	0.52	0.15	**0.001**
V4 (ml)	0.38	0.14	**0.011**
Corpus callosum			
Volume (ml)	−0.026	0.005	**0.008**
Length (mm)	0.002	0.025	0.94
Height (mm)	0.11	0.034	**0.003**
Thickness (mm)	−0.61	0.110	**<0.001**
Putamen			
Volume left (ml)	−0.85	0.18	**<0.001**
Volume right (ml)	−0.77	0.19	**<0.001**
Thickness left (mm)	−0.31	0.12	**0.011**
Thickness right (mm)	−0.42	0.11	**0.001**
Distance inner (mm)	0.14	0.043	**0.003**
Distance outer (mm)	0.07	0.046	0.156

Bold, significant after correction for multiple comparisons using FDR. Models with volume variables used brain scaling factor as a covariate while models with length, height, thickness, and distance variables used inner skull width as a covariate.

Table 5.

Association between longitudinal MRI measurements and CGG repeat length in premutation carriers ($N = 65$)

MRI Measurements	FXTAS Stage		CGG		CGG-Squared	
	β (SE)	FDR	β (SE)	FDR	β (SE)	FDR
Ventricles						
Lateral (ml)	3.44 (0.90)	**0.001**	3.52 (0.83)	**<0.001**	−0.016 (0.004)	**0.002**
Third (ml)	0.06 (0.03)	0.075	0.14 (0.03)	**<0.001**	−0.0006 (0.0002)	**0.002**
Fourth (ml)	0.04 (0.04)	0.261	0.12 (0.04)	**0.004**	−0.0059 (0.0002)	**0.007**
Corpus callosum						
Volume (ml)	−0.30 (0.14)	0.061	−0.040 (0.020)	0.053	-	-
Length (mm)	−0.12 (0.17)	0.509	0.065 (0.038)	0.093	-	-
Height (mm)	0.30 (0.14)	**0.006**	0.050 (0.022)	**0.038**	-	-
Thickness (mm)	−0.16 (0.04)	**0.001**	−0.028 (0.005)	**<0.001**	-	-
Putamen						
Volume left (ml)	−0.12 (0.03)	**0.001**	−0.052 (0.020)	**0.017**	0.0002 (0.0001)	**0.045**
Volume right (ml)	−0.08 (0.03)	**0.013**	−0.059 (0.017)	**0.007**	0.0002 (0.0001)	**0.032**
Thickness left (mm)	−0.12 (0.04)	**0.010**	−0.010 (0.003)	**0.003**	-	-
Thickness right (mm)	−0.16 (0.04)	**0.001**	−0.011 (0.003)	**<0.001**	-	-
Distance inner (mm)	0.28 (0.13)	0.061	0.26 (0.086)	**0.007**	−0.0012 (0.0005)	**0.016**
Distance out (mm)	0.03 (0.12)	0.080	0.27 (0.097)	**0.012**	−0.0014 (0.0005)	**0.017**

Bold, significant after correction for multiple comparisons using FDR. Models predicting volumes used brain scaling factor as a covariate while models predicting length, height, thickness, and distance used inner skull width as a covariate.